Errata

Errata if available for this printing may be obtained from ASNT's Web site, www.asnt.org, or as hard copy by mail, free on request from ASNT at the address above.

(26) $\quad a_1 = \sqrt{a^2 + j\omega\mu_r\mu_0\sigma}$

where a is the integration variable, $J_1(x)$ is the bessel function of the first kind and first order, l is the width of the coil (meter), l_0 is the liftoff (meter), r_1 is the inner radius of the coil (meter), r_2 is the outer radius of the coil (meter), μ_r is relative magnetic permeability (dimensionless), μ_0 is magnetic permeability (henry per meter) of free space and σ is conductivity (siemens per meter).

The eddy current density is calculated from the magnetic vector potential:

(27) $\quad J_\phi = -j\omega\sigma A_\phi$

In the case of a normal coil above a half-space conductor (Fig. 2a), the induced current density is as follows:

(28) $\quad J_\phi(r, z) = \dfrac{j\omega\sigma\mu_r\mu_0 NI}{l(r_2 - r_1)} \displaystyle\int_0^\infty \dfrac{J(r_1,r_2)}{a^2}$

$\qquad \times \left(e^{-a(l+l_0)} - e^{-al_0} \right)$

$\qquad \times \dfrac{e^{a_1 z} J_1(ar)}{a\mu_r + a_1} \, da$

where I is the root mean square of the coil current.

Equations 24 and 28 involve the numerical computation of an infinite integral. Numerical integration techniques available in most numerical analysis software packages can be used to calculate the integrals.

Figure 2b is a computer generated impedance display for a surface coil. The impedance is depicted normalized, using the inductive reactance of the coil in air as the normalizing factor. (This quantity can also be computed from Eq. 24 by setting conductivity to zero, $a_1 = a$). Such impedance displays demonstrate the optimum frequency for a specific test. This frequency is usually the one that produces the best phase difference between the loci of two parameters. The conducting half-space material is aluminum and the solid curve represents the locus produced by varying the excitation frequency. Because the conductivity and frequency always appear as a product in Eq. 22, the same curve would have been produced for a constant excitation frequency and a varying conductivity. The dashed lines are the liftoff curves and represent the impedance variation with coil liftoff. The dotted curves show the impedance variation with frequency for different magnetic permeabilities of the half-space material.
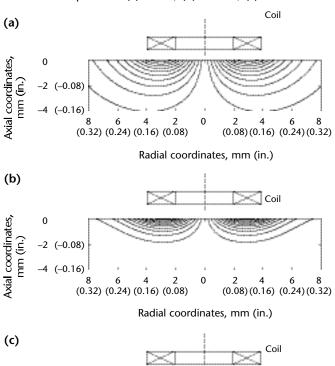
Figure 3 is an example of a computer generated display of eddy current contours induced by a surface coil at various frequencies. As expected, the higher frequencies result in a smaller penetration of the eddy currents in the conducting object. Using Eq. 28 for a variety of coils reveals that peak eddy current densities associated with larger coils fall off more slowly with depth than those produced by smaller coils. A similar investigation conducted by Mottl[19] showed that the standard depth of penetration and linear-with-depth phase delay, obtained as solutions for the plane wave case, very rarely approximate the eddy current distribution in conducting samples beneath a real coil. The standard depth of penetration remains a material parameter rather than a real measure of penetration.

The Dodd and Deeds models have been proven very useful because they were successful in predicting experimental data from eddy current measurements. Since the 1970s, they have been widely used by the nondestructive testing community in
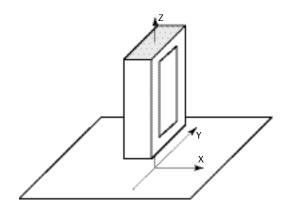
FIGURE 3. Contours of eddy currents induced by surface coil at various frequencies: (a) 1 kHz; (b) 10 kHz; (c) 100 kHz.

(a)

(b)

(c)
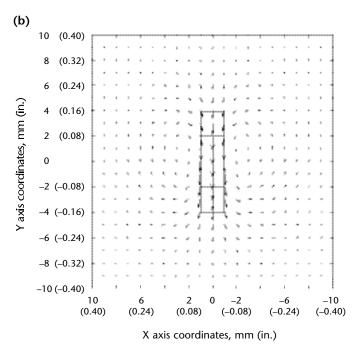
FIGURE 8. Eddy current testing with rectangular coil perpendicular to test object: (a) setup; (b) eddy current pattern.

(a)

(b)

X axis coordinates, mm (in.)

Conclusions

Analytical solutions in eddy current testing, although restricted to certain geometries as compared to the more general numerical solutions, have an explicit and closed form. The models are not computationally intensive and offer accurate solutions. They have limited scope but not limited value.

Whenever plausible, analytical solutions are preferable to numerical ones because they are easier to apply, are less expensive to compute, are more accurate and finally allow for easy parametric studies of the test geometry.

The geometry of the problem (Fig. 13) lends itself to the Schwarz-Christoffel theory,[87,88] which yields a conformal transformation to map the domain of the crack and the adjoining half plane above it into a half plane. An elementary solution for the half plane will lead to a fixed potential difference across the crack. Then, an inverse transform can be applied to produce a representation of the electric field at the crack mouth. In this case, a suitable analytic inverse transform is apparently lacking and the mapping must be done numerically by using, possibly, the newton-raphson iterative technique or the brent algorithm.[89]

Förster[90] and others[91] have used conformal mapping to determine the magnetic flux leakage at the crack mouth. In fact, the mapping is used widely to find the magnetic field at the gap between two pole pieces such as the field at the gap between the poles of a magnetic recording head.[92] In eddy current problems, the electric field is needed rather than the magnetic field but the solution is essentially the same (Fig. 13).

At the corners, the electric field is singular, varying in magnitude in air close to the corner as $(r_{corner})^{-1/3}$, where (r_{corner}) is the radial distance from the apex of the corner. This behavior is characteristic of the field in the vicinity of a right angled wedge.[93] Between the crack faces, the field tends to become more uniform deeper into the crack. The magnitude of the field between the faces depends on how deep and wide the crack is. If the crack is made narrower while the potential across the crack remains the same, then the magnitude of the electric field increases. In the limit of closure without contact, the electric field forms a singular layer, infinitely strong, of infinitesimal thickness. It is this limiting case that will be explored here because the singular layer has a simple mathematical representation.

Impenetrable Crack

In calculations of the field perturbation due to a crack, it is usual and convenient to apply a boundary condition that states that the normal component of the current density in the conductor at the crack face is zero. Although the surface of the crack supports a distribution of electrical charge and the charge must get there somehow, in the quasistatic approximation the charging current is neglected. In a conductor, the displacement current $j\omega\varepsilon_0 E$ is neglected because it is very much smaller than the charge current $\sigma_0 E$. Even at high eddy current test frequencies, ~10 MHz, where the magnitude of displacement current is greater than at lower frequencies, the ratio $\varepsilon_0\omega\cdot\sigma_0^{-1}$ is on the order of 10^{-9} for a low conductivity metal, 0.58 MS·m^{-1} (1 percent of the International Annealed Copper Standard). However, the accuracy of a boundary condition that neglects the charging current at the crack face is dependent on crack width. Therefore, it is necessary to seek a justification for the quasistatic approximation in this context.

The normal component of the true current, to use Maxwell's term for the sum of the displacement and charge current, is continuous across an interface. Therefore, the displacement current between the faces and directed across the crack is equal to the charging current at the conducting side of the crack face. Hence, the boundary condition is justified if the displacement current $j\omega\varepsilon_0 E_n$ across the crack is negligible compared with the tangential charge current $\sigma_0 E_t$ at the crack
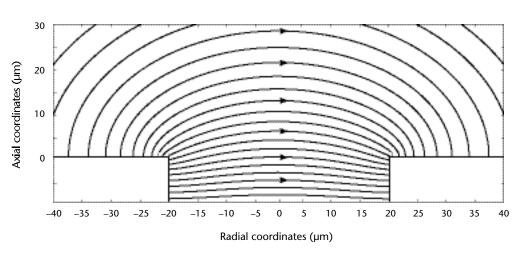

FIGURE 13. Electric field at crack opening.

coils) and pickup coil (or coils). In this case, the voltage induced across the pickup coils is measured.

Geometry

A third way to classify probes is according to geometry. Common probe designs include (1) inside diameter probes, (2) encircling coils (outside diameter probes), (3) surface probes such as pancake units and (4) special designs such as plus point probes. The pancake probe has a coil whose axis is normal to the surface of the test material and whose length is not larger than the radius. The plus point probe consists of two coils that lie at a right angle to each other.

Inside diameter probes consist of circular coils inserted in tubes or circular holes. Encircling coils are similar in structure to inside diameter probes except for the fact that the test material is passed inside the coils. They are primarily used to test the outside surface of round materials such as tubes and rods. Surface coils are some of the most widely used eddy current probes. In most cases, they consist of flat coils and are used to test flat surfaces or surfaces with relatively large curvatures relative to their size. Surface probes may be curved to fit contours of the test object.

All of these probes may be used in any of the configurations described above. Thus, for example, an inside surface probe may be absolute or differential and either the impedance or the induced voltage may be measured.

Factors Affecting Eddy Current Probes[1]

Liftoff Curve

An eddy current probe has an initial impedance (quiescent impedance) that depends on the design of the probe itself. This is an intrinsic characteristic of any eddy current probe and is sometimes called *infinite liftoff impedance*. As the probe is moved closer to the test object, the real and imaginary parts of the impedance begin to change until the probe touches the material surface. This is called the *zero liftoff impedance*. The impedance curve described by the probe as it moves between these two points is the liftoff curve and is a very important factor to consider in eddy current testing. Because of the nature of the eddy current probes, the curve is not linear (the change in the field is larger close to the coils). In many cases, especially with small diameter probes for which the field decays rapidly, the range in which measurements

may be taken is very small and the effect of liftoff can be pronounced. In other cases, such as with large diameter probes or with forked probes, the effect may be considerably smaller.

Liftoff, because it is troublesome in many cases, is often considered an effect to be minimized. Liftoff effects may be reduced by techniques such as surface riding probes[2] or compensated for by making multifrequency measurements.[3] At the same time, some important eddy current tests depend on the liftoff effect. Measurements of nonconductive coating thicknesses over conducting surfaces and testing for surface evenness are two such tests.

Fill Factor

For encircling coils, the coupling factor, analogous to the liftoff effect, is referred to as *fill factor*. Fill factor is a measure of how well the tested article fills the coil. The largest signal is obtained with the material completely filling the coil — fill factor is almost equal to 1.0. Although it is usually desirable to maximize fill factor, some tests rely on fill factor variations. Fill factor is determined by the intersection of the impedance curve with the vertical or imaginary axis of the impedance plane.

Depth of Penetration

When the eddy current probe is placed on the test object, the eddy currents induced in the test object are not uniformly distributed throughout the material. The eddy current density is high at the surface and decays exponentially with depth in the material; the phenomenon that accounts for this density difference is called the *skin effect*. A measure of the depth to which eddy currents penetrate the material is called the *depth of penetration,* or *skin depth. The standard depth of penetration* can be defined as:

$$(2) \quad \delta = \sqrt{\frac{1}{\pi f \mu_0 \mu_r \sigma}}$$

where f is frequency (hertz), δ is the standard depth of penetration (meter), μ_0 is the magnetic permeability of free space, μ_r is the relative magnetic permeability and σ is the conductivity of the material.

The standard depth of penetration is a convenient figure at which, under precisely controlled conditions, the eddy current density has decayed to $1 \cdot e^{-1}$ (37 percent) of its surface value. It is an important figure for practical purposes because, at about five standard depths of penetration (under precisely defined conditions), the eddy current density is less than 0.7 percent of the surface value.

measure 3.0 × 0.6 × 0.4 mm
(0.12 × 0.024 × 0.016 in.) and output
signals are generally larger than for hall
elements, although the response to field
intensity is not so linear for higher fields
as shown in Fig. 45.

Figure 46 shows that frequency
response is flat from direct current field to
3 kHz and Fig. 47 shows that sensitivity is
stable without temperature dependence in
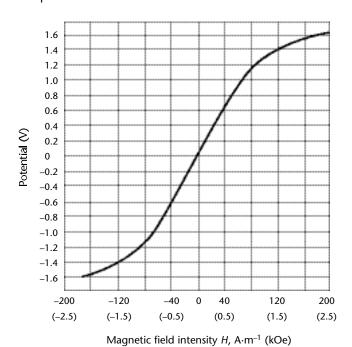the range of –10 to 50 °C (14 to 122 °F).

Magnetic Recording Tape

For the testing of flat plates and billets, it
is possible to scan the surface with wide
strips of magnetic recording tape.
Discontinuity signals are taken from the
tape by an array of tape recorder heads.
Elongated magnetic balloons also exist for
the testing of the inside surface of tubes.
Scale, dirt or oil on the test surface can
contaminate the tape. Surface roughness
can tear the tape.

Magnetic Particles

Magnetic particles are finely ground high
permeability magnetic material,
sometimes dyed for visible contrast with
the test surface. Ideal test conditions
occur when a fine spray of such particles
is intercepted by a magnetic flux leakage
field and some of them stick to the field.
An advantage over other forms of
magnetic indicators is that the particles

have zero liftoff from the discontinuity
field. In a simple approximation, the force
F_{mag} holds the particles in the leakage
field:

$$(20) \quad F_{mag} \quad = \quad \alpha \mu_0 V_{vol} \left(H \cdot \nabla \right) H$$

where ∇ is the vector differential operator
(gradient operator), H is the local flux
leakage field intensity (ampere per meter),
V_{vol} is the volume (cubic meter) of the
particle, α is a factor related to the
demagnetization factor of the particle and
μ_0 is the permeability of free space
($\mu_0 = 4\pi \times 10^{-7}$ H·m^{-1}).
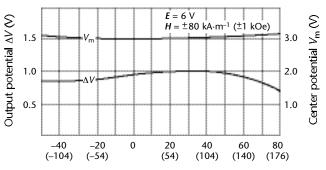
The force that holds the particle to the
discontinuity leakage field is proportional
to the result of a vector calculus operation
on the leakage field. This force can be
computed for simple leakage fields by
using approximations such as those by
Förster[28] and by Zatsepin and
Shcherbinin[29] or more accurately by using
finite element techniques such as those
described elsewhere, in this volume's
chapter on modeling. The force is also

FIGURE 46. Frequency response of magnetodiode at ambient
temperature of 25 °C (77 °F).

FIGURE 45. Response of magnetodiode is linear up to about
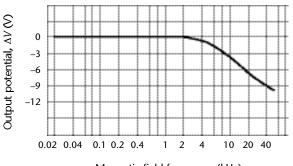40 kA·m^{-1} (500 Oe) at ambient temperature of 25 °C (77 °F)
and potential of 6 V.

FIGURE 47. Temperature dependence of magnetodiode.

PART 5. Eddy Current Imaging with Magnetooptic Sensors

Magnetooptic Imaging Principles

Magnetooptic imaging is a real time eddy current imaging technology that relies on the faraday magnetooptic effect. This technology has been used to image cracks and other discontinuities in electrical conductors such as aging aluminum airframes. The following discussion briefly describes such imaging devices and gives examples of both surface and subsurface indications obtained with this approach.

Both conventional and unconventional eddy current techniques rely on Faraday's law of electromagnetic induction:

$$(21) \quad \nabla \times E \;=\; -\frac{\partial B}{\partial t}$$

In differential form this law describes the connection between magnetic field vector B and electric field vector E at points of three-dimensional space at time t (second) — including points located inside electrical conductors.[31,32] In particular, this law shows that a time varying magnetic field B (produced by a moving permanent magnet, the field from a coil of wire carrying a changing current or some other source) in the vicinity of any electrical conductor having conductivity σ, will induce a time varying electric field E and thus a time varying eddy current density J at an arbitrary point near the surface of the conductor:

$$(22) \quad J \;=\; \sigma E$$

To gain a general understanding of the relevant relationships and concepts, consider the familiar case of a time varying magnetic field B produced by an external alternating current in a coil of wire.

By Lenz's law,[31] the direction of the vector J at any point in the conductor and hence the direction of the eddy currents is always opposed to the change in the direction of the external electric currents that produced B in the first place. This opposition is illustrated in Fig. 48, where a standoff or noncontact coil carrying an alternating current near a conducting plate has induced eddy currents in the plate. The magnetic fields in Fig. 48 tend to be excluded from the conducting plate, especially at high frequencies. The magnitude of the eddy currents diminish as the depth increases.
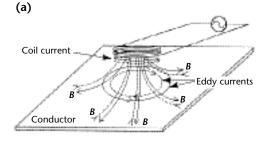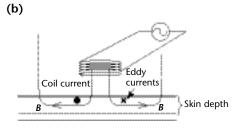
Sheet Eddy Current Generation

Coils similar to those in Fig. 48 form the basis for conventional coil based eddy current techniques. Note that the induced eddy currents form a kind of image of the coil currents in the conducting plate, meaning that the magnitude of the eddy currents is greatest just under the circular footprint of the coil. Consider an unconventional eddy current induction technique called *sheet current induction* as illustrated in Fig. 49.[33,34]

In Fig. 49, just as in the case of the coil of Fig. 48, Lenz's law ensures that the

FIGURE 48. Eddy currents being induced in electrically conducting plate by magnetic field B produced by coil of wire carrying alternating current: (a) view of eddy current distribution in plate; (b) view of eddy current penetration into plate. By Lenz's law, direction of induced eddy currents (current density $J = \sigma E$ at one point) is opposed to a change in direction of currents in coil (solid and dotted lines represent currents and fields roughly 180 degrees out of phase).

(a)

(b)
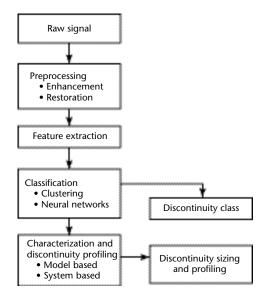
PART 1. Signal Enhancement

Signal and image processing techniques are valuable for the accurate and consistent interpretation of signals in nondestructive testing. Signal processing performs important functions in data analysis — ranging from simple noise filtering for enhancing the ratio of signal to noise to automated signal classification for improving discontinuity detectability. This chapter focuses on some of the more advanced signal processing techniques. Classical texts can provide a fundamental understanding of the subject.[1,2] A schematic diagram for the overall approach used in nondestructive test signal analysis is shown in Fig. 1.

Techniques of signal processing can be broadly classified into procedures for (1) enhancement, (2) restoration, (3) classification and (4) characterization. These techniques are described below.

Signal enhancement techniques are used to minimize high frequency noise and artifacts in a signal. These techniques generally do not require a precise understanding of the factors that contribute to the distortion. Techniques for enhancing the ratio of signal to noise can range from simple averaging and low pass filtering[1] to more sophisticated techniques such as wavelet shrinkage denoising. In general, the noise contained in a signal can be attributed to several sources, including instrumentation, probe wobble and variations in liftoff and surface roughness. Signals can be enhanced using simple standard linear low pass filters, band stop filters and band pass filters.[2] These filters are often implemented in either hardware or software and available as special features in the instrument. However, these filters are effective only when the signal is stationary. A signal is considered stationary when its statistical properties such as mean or variance do not vary with time. Nondestructive test signals that contain time localized discontinuity indications are, as a rule, nonstationary. Such problems are addressed using techniques such as wavelet shrinkage denoising,[3] described next.

FIGURE 1. Overall approach for signal analysis in nondestructive testing.

Wavelet Shrinkage Denoising Filter

Consider a noisy signal y_i represented by the discrete time sequence:

$$(1) \quad y_i = x_i + \sigma z_i$$

where $i = 0, 1, ..., n{-}1$; subscript i is the time index of the signal; n is the length of the time sequence; x_i is the desired signal; and z_i represents conventional white noise (indicating that the noise is uncorrelated[1,2]) with standard deviation σ. The discrete wavelet transform decomposes a signal y into a weighted sum of basis functions $\psi_{v,k}$:

$$(2) \quad y(n) = \sum_v \sum_k c_{v,k} \psi_{v,k}(n)$$

where v and k are integer values. The basis functions $\psi_{v,k}$ are derived by using dilations and translation operations from a single function ψ, referred to as the *mother wavelet*:

$$(3) \quad \psi_{v,k}(n) = 2^{-\frac{v}{2}} \psi\left[2^{-\frac{v}{2}}(n-k) \right]$$

(24) $\quad c(k) \;=\; \sqrt{\dfrac{2}{N}}$

for $1 \le k < N - 1$.

This technique results in a feature vector composed of a smaller number of coefficients B_k that can represent the signal.

Discrete Wavelet Transform

The discrete wavelet transform[9] of a signal $x(n)$ is a joint time scale transform that provides both time and frequency localization of a signal. The discrete wavelet transform can be expressed as the weighted sum of basis functions:

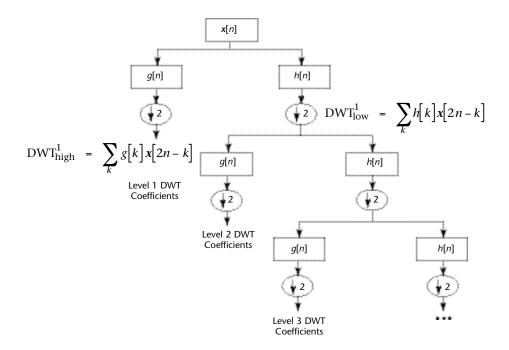**(25)** $\quad x(n) \;=\; \displaystyle\sum_v \sum_k C_{v,k}\,\psi_{v,k}(n)$

where realizations of the wavelet basis function $\psi_{v,k}(n)$ are derived from a single function $\psi(n)$, referred to as the *mother wavelet,* by dilations v and translations k according to:

(26) $\quad \psi_{v,k}(n) \;=\; 2^{-\frac{k}{2}}\,\psi\!\left[2^{-k}(n-k)\right]$

The discrete wavelet transform coefficients $C_{v,k}$ are determined by projecting the signal $x(n)$ onto the wavelet basis set $\psi_{v,k}(n)$. It is usually implemented as a series of subband filters. The most common version is the two-band discrete wavelet transform, which uses two finite impulse response filters — a low pass filter and a high pass filter.

The computation of the discrete wavelet transform coefficients for a data vector x of length n (where n indicates the number of points in the signal) is indicated in Fig. 8, which presents a fast implementation of the discrete wavelet transform using a filter bank approach. The output of each filter is downsampled by a factor of 2 by discarding every other sample. The output of the high pass filter represents the discrete wavelet transform coefficients at the first resolution level. The output of the low pass filter is then applied to the same set of filters and sampled again. The output of the high pass filter is retained as the discrete wavelet transform coefficients at the

FIGURE 8. Filter bank approach for discrete wavelet transform computation.[9]

$$\mathrm{DWT}^1_{\mathrm{high}} \;=\; \sum_k g[k]\,x[2n-k]$$

$$\mathrm{DWT}^1_{\mathrm{low}} \;=\; \sum_k h[k]\,x[2n-k]$$

Level 1 DWT Coefficients

Level 2 DWT Coefficients

Level 3 DWT Coefficients

Legend
DWT = discrete wavelet transform
g = high pass function
h = low pass function
k = iteration number
n = number of points in signal
x = data vector

second resolution level. This process is repeated until the number of samples is reduced to 1. The number of possible resolution levels is given by α:

$$(27) \quad \alpha \;=\; \log_2 n$$

Because the discontinuity related information is typically present in the discontinuity scale subspace, an appropriate set of coefficients in the discontinuity subspace can be used as features.

Principal Component Analysis

Principal component analysis is a statistical technique that linearly transforms a time series sequence into a substantially smaller set of uncorrelated variables that contains most of the information in the original data set.[10] The overall goal of principal component analysis is to reduce the dimensionality of the original data set. Principal component analysis allows the reconstruction of the original pattern from linear projections required to have sequentially maximal variances. The basis vectors of the representation are constrained to be mutually orthonormal. If X is an $n \times n$ data matrix of measurement vectors with mean M_x and covariance matrix Σ_x (where subscript x represents a datum) an orthogonal set of eigenvectors may be found that diagonalizes the covariance matrix. By arranging the eigenvectors in a matrix in accordance with decreasing eigenvalues (largest first), an ordered orthogonal basis may be created that has the greatest degree of variability of the data along the first eigenvector. Retaining only p largest eigenvalues provides a feature extraction operator Φ, a $p \times p$ matrix of p eigenvectors. Using this transformation matrix, a data set X may be transformed to matrix Y:

$$(28) \quad Y \;=\; \Phi\big(X - M_X\big)$$

making Y an orthonormal projection of X onto the columns of the transformation matrix. The inverse transformation may be used to reconstruct the original data set X by:

$$(29) \quad X \;=\; \Phi^{\mathrm{T}} Y + M_X$$

where Φ^{T} represents the transpose of matrix Φ. The matrix Y represents X in the domain spanned by the vectors ϕ_1, ..., ϕ_p. These columns of Y are referred to as the *principal components* of the data set X and are of a lower dimension than the original data vectors.

Linear Predictive Coding Coefficients

Linear predictive modeling[11] is commonly used in the processing of speech signals. Linear predictive coding coefficients are known to accurately represent speech signals with a small set of parameters. The approach can be used also for extracting features from test signals.

In linear predictive coding analysis, it is assumed that the present value of the sample $s(n)$ can be represented as a weighted sum of the past samples. The linear predictive coding coefficients are estimated by minimizing the mean squared error between the predicted value and true value. The error $\varepsilon(n)$ is given by:

$$(30) \quad \varepsilon(n) \;=\; s(n) - \sum_{j=1}^{p} \alpha_j\, s(n-j)$$

where α_j represents the estimates of the linear predictive coding coefficients. Setting the partial derivatives of the mean squared error with respect to α_j to zero for $j = 1, 2, ..., p$ gives:

$$(31) \quad E\left\{ \left[s(n) - \sum_{j=1}^{p} \alpha_j\, s(n-j) \right] s(n-i) \right\} = 0$$

for $i = 1, 2, ..., p$. Equation 31 can be rearranged:

$$(32) \quad \sum_{j=1}^{p} \alpha_j\, \phi_n(i,j) \;=\; \phi_n(i,0)$$

for $i = 1, 2, ..., p$, where ϕ_n is the autocorrelation function:

$$(33) \quad \phi_n(i,j) \;=\; E\big\{ s(n-i)\, s(n-j) \big\}$$

The linear predictive coding coefficients in Eq. 33 can be solved recursively by using Durbin's algorithm.[11] Nondestructive test signals can be represented by a small set of linear predictive coding coefficients, thereby achieving data reduction and compaction. The coefficients represent the signal and serve as a reduced dimensional feature vector.

Feature Evaluation

Once the features are computed, a feature evaluation and selection step may be used to eliminate redundancy in the representation and to evaluate the features on the basis of the discriminatory information. More importantly, the

PART 3. Signal Characterization

Signal characterization involves a more complete solution to the inverse problem. In material science, the inverse problem involves reasoning from effects (that is, indications) in order to draw inferences about test objects. Characterization techniques use information contained in the signal to estimate the size, shape and location of discontinuities. In other words, characterization procedures involve the full two-dimensional or three-dimensional reconstruction of discontinuity profiles in terms of the spatial distribution of the material properties of the test object. In general, the objective of the signal or discontinuity characterization procedure can be described as the identification of a mapping f such that:

$$(43) \quad D \;=\; f\!\left(S\right)$$

where S represents the measurement vector from a scan in two dimensions M and Q:

$$(44) \quad S \;=\; \left\{s_{ij}\right\}_{M \times Q}$$

and D represents the discontinuity profile:

$$(45) \quad D \;=\; \left\{d_{ij}\right\}_{R \times P}$$

The value of d_{ij} represents the depth of the discontinuity at a location (i,j).

Several approaches have been developed for solving the inverse problem in nondestructive testing. These solutions can be categorized as either phenomenological or nonphenomenological. Phenomenological techniques are based on the underlying physical process of the nondestructive test technique. Examples of the phenomenological approach for inversion are based on analytical solutions of the underlying governing equation, which is in general a difficult problem. Nonphenomenological approaches do not depend on the physics of the inspection technique. These approaches model the nondestructive test system as a black box or as a linear system and use signal processing techniques to invert the measured signal. Typical signal processing approaches for inversion use neural networks for solving the discontinuity characterization problem. An approach using a radial basis function neural network for the inversion of magnetic flux leakage signals is described next.[20]

Radial Basis Function Networks

Radial basis function networks can be viewed as tools for multivariate interpolation.[20] Such networks can be used for estimating a hypersurface that provides what can be called the *best fit* to the training data. The architecture of the radial basis function network is in many respects similar to that of a multilayer perceptron, defined above. A nonlinear transformation of the signal is performed between the input and hidden nodes followed by a linear transformation between the hidden and output nodes. Mathematically, the radial basis function network computes a multidimensional function:

$$(46) \quad f\!\left(x\right) \;=\; \sum_{i=1}^{N} w_i\, \phi_i\!\left(\left\|x - c_i\right\|\right)$$

where ϕ_i is a set of basis functions, c_i are the basis centers and w_i are the weights. Substituting the values in the training data $\{x_i,\, f(x_i),\, i \;=\; 1,\, \ldots,\, N\}$ in Eq. 46 makes it possible to derive the matrix equation:

$$(47) \quad f \;=\; \Phi\, w$$

The training of the radial basis function network consists of estimating the expansion coefficients, which can be done by inverting Eq. 47:

$$(48) \quad w \;=\; \Phi^{-1} \cdot f$$

Once the weights are estimated by using the training data, the radial basis function network can be used to invert a test signal x according to Eq. 46.

Reconstruction results can be further improved by using a variation of the radial basis function network, a multiresolution approach that uses neural networks with wavelet basis functions.[21]

13

C H A P T E R

Electromagnetic Techniques for Material Identification

Timothy E. Kinsella, Dassault Falcon Jet, Teterboro, New Jersey

Donald J. Hagemaier, Huntington Beach, California (Part 2)

Johann H. Hinken, Hochschule Magdeburg-Stendal, Magdeburg, Germany (Part 6)

George Mordwinkin, Sensor Corporation, Scottdale, Pennsylvania (Parts 5 and 6)

Andrew P. Washabaugh, Jentek Sensors, Waltham, Massachusetts (Part 7)

Markus Zahn, Massachusetts Institute of Technology, Cambridge, Massachusetts (Part 7)
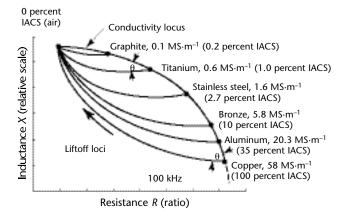
Conductivity and Permeability Loci on Impedance Plane[4]

The impedance plane response to the different conductivities of various nonmagnetic alloys is shown in Fig. 4. The material points trace out a characteristic comma shaped curve with conductivity increasing in a clockwise direction. The coil liftoff loci are shown for the different metals. Note that the separation angle between the conductivity locus and the liftoff locus is much smaller for titanium than it is for copper. Hence the unwanted liftoff variable will affect test results less when testing copper or aluminum alloys at 100 kHz than it will when testing titanium or graphite.

The material points are spaced around the conductivity locus in a nonlinear fashion. For example, the spacing between titanium and stainless steel at the top of the curve is much greater than it is between bronze and aluminum at the bottom of the curve.

Figure 5 shows the effect of test frequency on the conductivity and liftoff curves for nonmagnetic alloys. Frequency changes shift the points along the conductivity locus in a nonlinear fashion. This phenomenon, also true for other impedance curves, can be used advantageously because it allows the material points to be located for optimum response or suppression. Specifically a frequency should be chosen that causes the material points for the variables to be measured to move in a substantially different direction from those points to be suppressed.

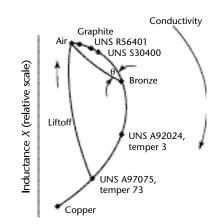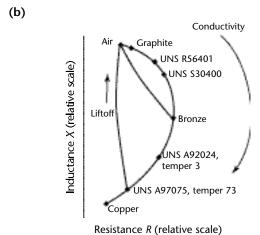**FIGURE 4.** Conductivity and liftoff loci on impedance plane.

Legend
IACS = International Annealed Copper Standard
θ = curve of separation between liftoff curve and conductivity curve
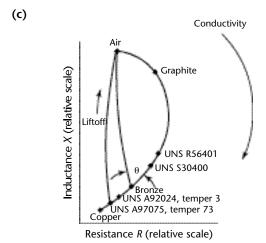
FIGURE 5. Movement of material points by frequency changes: (a) low frequency, 20 kHz; (b) medium frequency, 100 kHz; and (c) high frequency, 1 MHz.

(a)

(b)

(c)

Legend
UNS A92024 = Unified Numbering System A92024 heat treatable wrought aluminum alloy
UNS A97075 = Unified Numbering System A97075 heat treatable wrought aluminum alloy
UNS R56401 = Unified Numbering System R56401 titanium alloy
UNS S30400 = Unified Numbering System S30400 austenitic chromium nickel stainless steel

Table 1 lists the conductivity ranges for many of the aluminum alloys commonly used in aircraft structural applications. These data represent a composite of values from various airframe manufacturers and government agencies. The ranges include all values obtained for standard heat treatments except for extreme values obtained from one or two sources clearly outside the ranges of all other lists. Any time a conductivity value is obtained for an aluminum alloy and temper outside of the applicable range, its mechanical properties should be considered suspect.

An aluminum alloy has the highest conductivity and lowest strength when it is in the fully annealed temper. After quenching from the solution heat treatment temperature, the strength is increased and the conductivity is decreased. Many aluminum alloys are unstable after solution heat treatment even if held at room temperature. During this time, a certain amount of atom migration takes place to initiate the formation of submicroscopic particles. This process, sometimes called *natural aging*, increases the strength of the alloy but either has no effect on conductivity or causes a slight decrease in conductivity. Some aluminum alloys remain unstable for such long periods after quenching that they are never used in the solution heat treated condition — for example, Unified Numbering System A97075 wrought aluminum alloy.

If a solution heat treated alloy is precipitation hardened by heating at relatively low temperature, between 93 and 232 °C (200 and 450 °F), alloying atoms form small particles. At a critical size and distribution of particles, the strength of the aluminum alloy reaches a maximum. Conductivity increases during the precipitation hardening or artificial aging process. If aging is carried beyond the point where optimum strength is obtained, the strength will decrease but conductivity will continue to increase. Figure 12 shows the relationship between conductivity and strength for a typical structural aluminum alloy.

Variations from specified heat treatment practice can result in aluminum alloys with strengths below required levels. Heat treatment discrepancies

TABLE 1. Ranges of electrical conductivity for aluminum alloys.

| Alloy and Temper[a] | | Electric Conductivity | | | |
| Unified Numbering System (UNS) | Aluminum Association (AA) | Minimum | | Maximum | |
		MS·m⁻¹	(%IACS[b])	MS·m⁻¹	(%IACS[b])
UNS A91100	AA 1100	33.1	(57.0)	36.0	(62.0)
UNS A92014, untempered	AA 2014-0	28.1	(48.5)	29.9	(51.5)
UNS A92014, temper 3XX	AA 2014-T3XX	18.3	(31.5)	20.3	(35.0)
UNS A92014, temper 4XX	AA 2014-T4XX	18.3	(31.5)	20.3	(35.0)
UNS A92014, temper 6XX	AA 2014-T6XX	21.5	(37.0)	24.1	(41.5)
UNS A92019, untempered	AA 2219-0	24.9	(43.0)	26.7	(46.0)
UNS A92019, temper 3XX	AA 2219-T3XX	15.7	(27.0)	18.0	(31.0)
UNS A92019, temper 62X	AA 2219-T62X	18.0	(31.0)	20.6	(35.5)
UNS A92019, temper 8XX	AA 2219-T8XX	18.0	(31.0)	20.6	(35.5)
UNS A92024, untempered	AA 2024-0	26.4	(45.5)	29.0	(50.0)
UNS A92024, temper 3XX	AA 2024-T3XX	16.2	(28.0)	19.1	(33.0)
UNS A92024, temper 4XX	AA 2024-T4XX	16.5	(28.5)	18.9	(32.5)
UNS A92024, temper 6XX	AA 2024-T6XX	20.3	(35.0)	23.8	(41.0)
UNS A92024, temper 8XX	AA 2024-T8XX	20.9	(36.0)	24.7	(42.5)
UNS A93003	AA 3003	25.8	(44.5)	29.0	(50.0)
UNS A96061, untempered	AA 6061-0	27.3	(47.0)	29.6	(51.0)
UNS A96061, temper 4XX	AA 6061-T4XX	20.6	(35.5)	24.1	(41.5)
UNS A96061, temper 6XX	AA 6061-T6XX	23.2	(40.0)	26.1	(45.0)
UNS A97075, untempered	AA 7075-0	25.5	(44.0)	27.8	(48.0)
UNS A97075, temper 6XX	AA 7075-T6XX	17.4	(30.0)	20.3	(35.0)
UNS A97075, temper 73X	AA 7075-T73X	22.0	(38.0)	24.7	(42.5)
UNS A97075, temper 76X	AA 7075-T76X	20.9	(36.0)	22.6	(39.0)
UNS A97178, untempered	AA 7178-0	24.9	(43.0)	27.3	(47.0)
UNS A97178, temper 6XX	AA 7178-T6XX	16.8	(29.0)	19.7	(34.0)
UNS A97178, temper 76	AA 7178-T76	20.3	(35.0)	22.6	(39.0)

a. *X*s represent numerals unspecified in this list.
b. Percentage of International Annealed Copper Standard.